

Simulating radiative shocks in nozzle shock tubes

B. van der Holst^{a,*}, G. Tóth^a, I.V. Sokolov^a, L.K.S. Daldorff^a, K.G. Powell^b, R.P. Drake^a

^a*Department of Atmospheric, Oceanic and Space Sciences, University of Michigan, Ann Arbor, MI 48109, USA*

^b*Department of Aerospace Engineering, University of Michigan, Ann Arbor, MI 48109, USA*

Abstract

We use the recently developed Center for Radiative Shock Hydrodynamics (CRASH) code to numerically simulate laser-driven radiative shock experiments. These shocks are launched by an ablated beryllium disk and are driven down xenon-filled plastic tubes. The simulations are initialized by the two-dimensional version of the Lagrangian Hyades code which is used to evaluate the laser energy deposition during the first 1.1 ns. The later times are calculated with the CRASH code. This code solves for the multi-material hydrodynamics with separate electron and ion temperatures on an Eulerian block-adaptive-mesh and includes a multi-group flux-limited radiation diffusion and electron thermal heat conduction. The goal of the present paper is to demonstrate the capability to simulate radiative shocks of essentially three-dimensional experimental configurations, such as circular and elliptical nozzles. We show that the compound shock structure of the primary and wall shock is captured and verify that the shock properties are consistent with order-of-magnitude estimates. The produced synthetic radiographs can be used for comparison with future nozzle experiments at high-energy-density laser facilities.

Keywords: Radiative shocks, Radiation transfer, shock waves

1. Introduction

In the experiments of the CRASH project, high-energy-density plasma flow is driven by a beryllium disk irradiated by the Omega laser beams. The ablation of part of the beryllium results in a rocket launch of the remaining beryllium driving a strong shock-wave through a xenon-filled plastic tube. The shock heats the xenon gas to sufficiently high temperature so that it will ionize and create free electrons. Directly behind the shock the electrons and ions will equilibrate due to the Coulomb collisions. This will heat the electrons. The shock is fast enough so that the electrons have to emit radiation behind the shock in order to satisfy the energy balance equation. This results in a radiative cooling layer [1]. The transport of the radiation ahead of the shock will heat and ionize the xenon in the radiative precursor. Some fraction of the radiation in the upstream region will also transport sideways and strike the plastic tube. These photons can heat the plastic ahead of the primary shock. The ablated plastic that moves then inward compresses the xenon resulting in a so-called wall shock [2, 3]. It is the interplay between the primary and wall shock that is of interest for the CRASH project.

To model the laser-plasma physics and laser energy deposition in the radiative shock tube experiments, we use H2D, the 2D version of the Hyades code [4], which contains a built-in laser package. H2D is a Lagrangian radiation-hydrodynamics code that utilizes the axisymmetry. Hyades is capable of tracing rays in 3D; the runs shown below used 2D ray tracing for the laser energy deposition. We use the H2D code to simulate our experiments for the first 1.1 ns (sometimes up to 1.3 ns), the time of the full width half maximum (FWHM) 1 ns laser pulse including ramp-up and ramp-down time. The spatial profile of the beam is determined using a model for the irradiance pattern of the laser beams in typical experiments. At 1.1 ns the experiment is in a regime that is well described by radiation-hydrodynamics so that the simulation can be continued with the CRASH code [5] instead. This code solves for the multi-material hydrodynamic equations with a multi-group flux-limited diffusion model for the radiation and uses the

*Corresponding author

Email address: bartvand@umich.edu (B. van der Holst)

recently developed Block Adaptive Tree Library (BATL) [6]. We are currently constructing a laser package in our simulation code as an alternative to H2D and the progress in that work will be reported elsewhere.

The main goal of the CRASH project is to assess and to improve the predictive capability of a simulation code, based on the combination of experiments, simulation studies and statistical analysis. The baseline experiment is a laser-driven shock launched through a xenon-filled straight tube. We plan to perform an experiment in which the tube geometry is changed to contain a circular nozzle. These experiments and the comparison with the simulations will demonstrate how well the numerical code can predict the shock properties of the following experiment in which a wide circular tube tapers into an elliptical tube. In this project we plan to analyze the radiative shock structures in nozzle shock tubes in the context of predictive capability and uncertainty quantification of the simulations [7]. The demonstration that such numerical simulations are feasible is the topic of the present paper.

This paper is organized as follows. Section 2 describes the radiative shocks produced in nozzles with circular cross-section. We contrast the results with order-of-magnitude estimates based on physical arguments. Section 3 demonstrates the radiative shocks in nozzles with an elliptical neck. This simulation is fully three-dimensional. The paper concludes with Section 4.

2. Circular nozzle

A laser pulse irradiates a $20\ \mu\text{m}$ thick beryllium disk with $0.35\ \mu\text{m}$ wavelength light for the FWHM duration of 1 ns and with a laser energy deposition of 4 kJ. For the laser spot size we use a FWHM $800\ \mu\text{m}$ diameter which is smaller than the $1200\ \mu\text{m}$ diameter of the tube. We are currently constructing a laser package in the CRASH code, but the runs reported here use the Lagrangian radiation-hydrodynamics code Hyades 2D (H2D) [4] to evaluate the laser energy deposition during the first 1.1 ns which includes the laser ramp-up and ramp-down time. While our aim is to simulate radiative shocks in nozzles, the first 1.1 ns is however simulated in a straight tube for convenience. Calculating the first 1.1 ns with a straight tube and then transforming this tube into a nozzle is physically justified as long as the taper and shaft of the nozzle does only alter the radiative precursor. The justification originates from the observation that the radiative transport from the precursor back through the shock front is negligible [8]. The considered straight tube does have a cylindrical polyimide wall of $100\ \mu\text{m}$ thickness and inner radius of $600\ \mu\text{m}$ filled with xenon with mass density $\rho = 0.0065\ \text{g/cm}^3$, while there is vacuum outside. The beryllium disk is immediately to the left of $x = 0$, where x is the coordinate along the tube. The laser light will come in from the negative x direction. We place a gold washer next to the beryllium disk to protect the outside of the plastic tube from the laser light and use acrylic in between the gold and polyimide tube.

After 1.1 ns of simulation time the output of H2D is used to initialize the Eulerian CRASH code as described in Appendix A. The straight tube of H2D is transformed into a nozzle, see the left panel of Fig. 1 for one quarter of the nozzle domain. This nozzle changes cross-section in the following way. For $x < 500\ \mu\text{m}$ we do not modify the tube as defined in H2D. For $x > 750\ \mu\text{m}$ we shrink the tube diameter from $1200\ \mu\text{m}$ to $600\ \mu\text{m}$ and the polyimide wall thickness corresponding reduces to $50\ \mu\text{m}$. Between $500\ \mu\text{m}$ and $750\ \mu\text{m}$ the tube diameter and wall thickness are linearly shrinking (In the notation of Appendix A we use $x_0 = 500\ \mu\text{m}$, $x_1 = 750\ \mu\text{m}$, $\varepsilon_y = 1/2$ and $\varepsilon_z = 1/2$). The vacuum outside the nozzle is replaced with low density polyimide to avoid the otherwise zero mass density. The left panel of Fig. 1 shows the materials that are present in the simulation in color: beryllium (blue), polyimide (green), acrylic (red), and gold (yellow). The xenon inside the nozzle is for convenience not shown in this figure.

The computational domain size is $-150 < x < 3900$, $0 < y < 900$ and $0 < z < 900$ in microns, where y and z are the two directions transverse to the nozzle. The simulation is performed with an effective resolution of $2560 \times 512 \times 512$ grid cells using two levels of refinement. The effective cell sizes are therefore approximately $1.6\ \mu\text{m}$ along the tube and $1.8\ \mu\text{m}$ in the two transverse directions. The domain is decomposed in $4 \times 4 \times 4$ grid blocks. The mesh is refined at all interfaces that involve xenon or gold. To capture the shock front and the cooling layer, the mesh is also refined where the xenon density exceeds $0.02\ \text{g/cm}^3$. Grid blocks are also refined if these criteria are satisfied in the ghost cells.

We perform the simulations with the CRASH radiation hydrodynamics code [5]. This code solves for the radiation hydrodynamic equations in three operator splitting steps: (1) an explicit time step of the hydrodynamic equations using a shock-capturing solver, (2) a linear advection of the radiation bins in frequency-logarithm space, and (3) an implicit solve of the radiation diffusion, heat conduction, and energy exchanges. This code is continuously undergoing

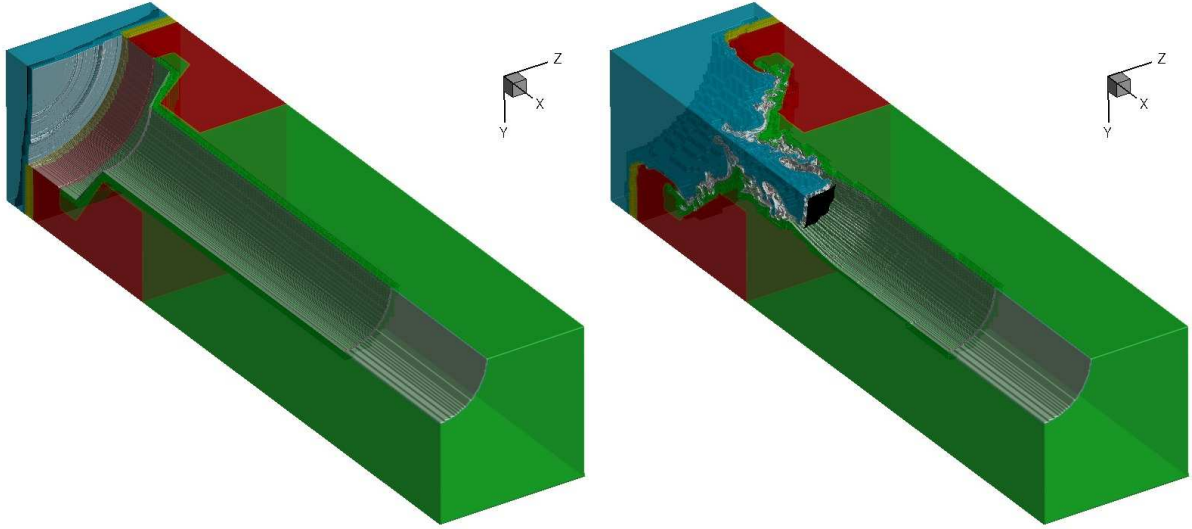


Figure 1: The materials in the 3D circular nozzle experiment at 1.1 ns (left panel) and 13 ns (right panels). Only one quarter of the shock tube is shown. The materials are beryllium (blue), polyimide (green), acrylic (red) and gold (yellow). The xenon inside the tube is not colored, but the border of the xenon volume is indicated by the white surface. The primary shock at 13 ns is depicted by a black iso-surface.

improvements. One such improvement is the resolution change treatment for the radiation diffusion and electron heat conduction, see Appendix C. During the simulations of the nozzles these improvements were not yet present and the original scheme in [5] was used instead. We use for the hydrodynamic part of the equations the HLLC scheme with a Courant-Friedrichs-Lewy number of 0.8 and the generalized Koren limiter with $\beta = 3/2$. For the radiation, we use the multi-group flux-limited diffusion model with 30 groups. The photon energy range is 0.1 eV to 20 keV that is logarithmically distributed over the groups. The radiation diffusion, heat conduction and energy exchanges are solved with the split (decoupled) implicit solver of [5] using the conjugate gradient method with a Schwarz-type Incomplete Upper-Lower (ILU) preconditioner.

Due to the symmetry in the problem we only need to simulate one quarter of the nozzle domain ($y > 0$ and $z > 0$) and use reflective boundary conditions at $y = 0$ and $z = 0$. For all other boundaries of the domain we use extrapolation with zero gradient. For the radiation we use zero albedo boundary conditions.

We simulated the shock evolution from 1.1 ns to 13 ns physical time. It took a little over three days to compute on 1000 cores of the HERA supercomputer at the Lawrence Livermore National Laboratory. The number of cells in the computational domain increased from 26.5 million at the beginning to about 38 million near the end. The 3D material identity at 13 ns is shown in the right panel of Fig. 1. The beryllium has moved into the nozzle and is like a piston driving a shock in the xenon. This shock is indicated by a black iso-surface (of high ion temperature values). The xenon itself is not shown but the edge of the xenon is emphasized by a white color to make the xenon entrainment between the beryllium and polyimide more clear. We can also see the inward moving polyimide which will lead to a wall shock. In the following we will analyze the shock structure in more detail and check if the results are in agreement with back-of-the-envelope estimates presented in [9, 8].

The shock structure in the xy -plane at time 13 ns is shown in Fig. 2. The top left panel is for the material identification of beryllium (blue), xenon (black), polyimide (green), gold (yellow) and acrylic (red). The nozzle with inner radius of $600 \mu\text{m}$, taper, and shaft with inner radius of $300 \mu\text{m}$ are visible. The black lines indicate the resolution changes between the grid refinement levels. The top right panel shows the mass density. Part of the polyimide is of very low density and represents vacuum. The dense polyimide tube thickness ranges from 50 to $100 \mu\text{m}$. The xenon is compressed by the beryllium piston flow resulting in a primary shock that is located at $x \approx 1700 \mu\text{m}$. For convenience we have indicated with black lines where the material interfaces are.

To check the obtained properties of the primary shock we first determine the beryllium piston velocity. For a 1 ns laser pulse of 4 kJ energy, the irradiance on a $800 \mu\text{m}$ diameter spot size is $8 \times 10^{14} \text{ W/cm}^2$. Most of this light will be

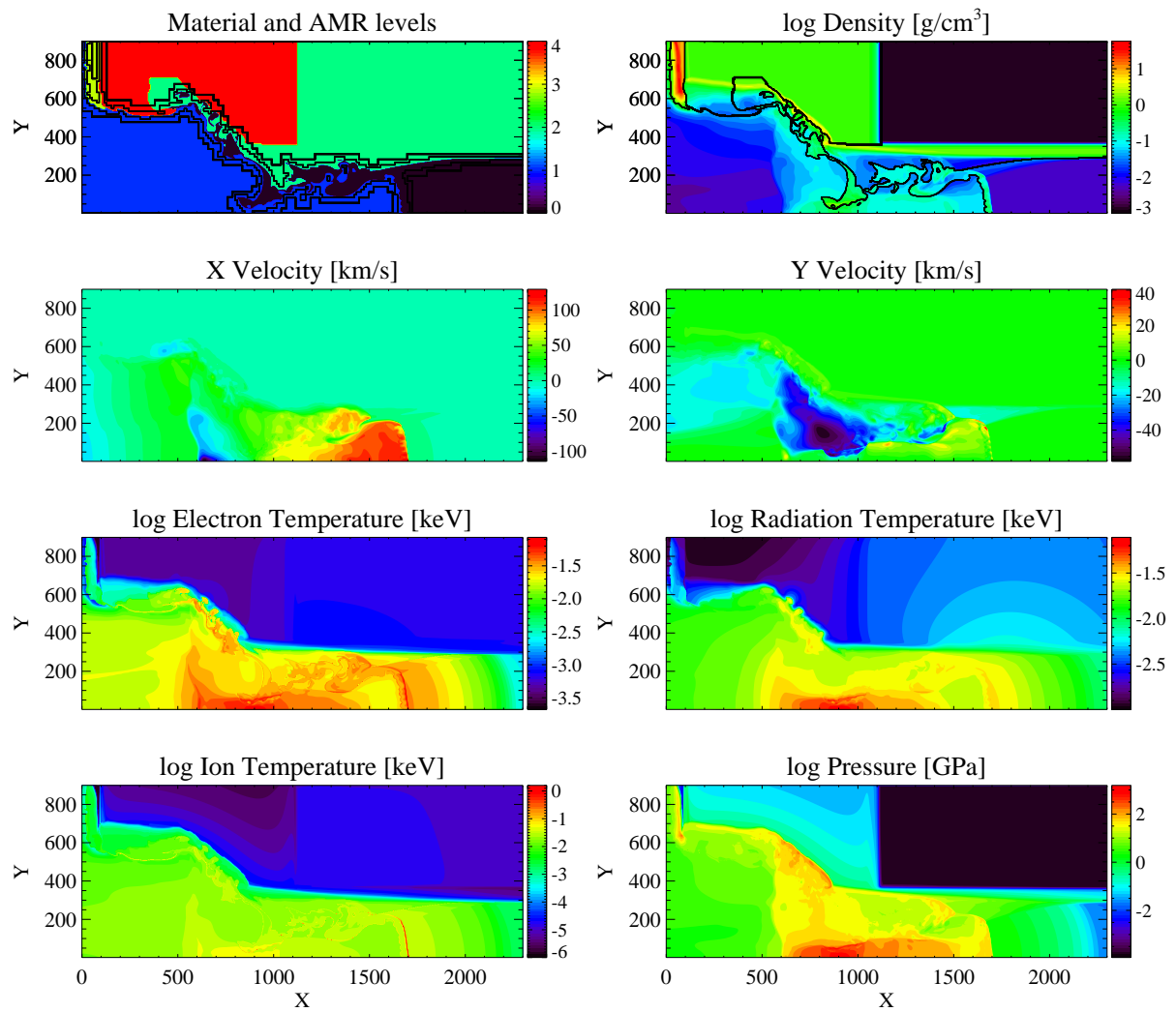


Figure 2: The radiative shock structure in the 3D circular nozzle simulation at 13 ns. The plots show in color contour the plasma and radiation state indicated in the plot titles as a function of the x and y positions in microns. The colors in the top left panel indicate beryllium (blue), xenon (black), polyimide (green), gold (yellow) and acrylic (red). The black lines in this panel show resolution changes, while in the top right panel the lines indicate the material interfaces.

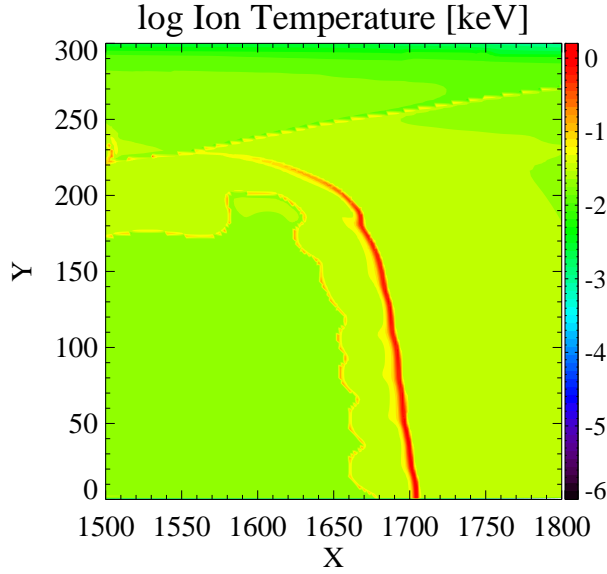


Figure 3: Zoom-in of the ion temperature near the shock with the x and y coordinates in microns.

absorbed in the beryllium, so that the absorbed energy per unit of area during this 1 ns is $8 \times 10^5 \text{ J/cm}^2$. About 20% of the beryllium mass, corresponding to $4 \mu\text{m}$ of the $20 \mu\text{m}$, will be ablated by the laser [8]. The ablation efficiency, which is the ratio of the kinetic energy of the remaining $16 \mu\text{m}$ beryllium to the total kinetic energy and exhaust, is to lowest order in the ablation percentage equal to the fraction of the mass that initially has been ablated, i.e. the efficiency is 20%. In reality, however, about half of the incident laser light reaches the beryllium above the absorption region where ablation occurs, while the other half is absorbed below the critical density. The actual efficiency from converting laser energy to kinetic energy of the remaining $16 \mu\text{m}$ of beryllium is therefore roughly 10%. The areal mass density of $16 \mu\text{m}$ beryllium at 1.8 g/cm^3 is approximately $3 \times 10^{-3} \text{ g/cm}^2$. The areal kinetic energy density $0.1 \times 8 \times 10^5 \text{ J/cm}^2$ corresponds therefore to an initial velocity of the beryllium of a little more than $v = 200 \text{ km/s}$. This beryllium will launch a shock through the xenon-filled tube. This high velocity is only achieved at early times. The numerically obtained shock velocity gradually reduces to a value between 110 km/s and 120 km/s at time 13 ns as shown in the X velocity plot of Fig. 2.

The unshocked xenon gas pressure is initially about 1.1 atm while the density is $\rho = 6.5 \times 10^{-3} \text{ g/cm}^3$. With the above mentioned shock velocity of $v \approx 110 \text{ km/s}$ we obtain a xenon post-shock pressure at 13 ns of the order of $\rho v^2 \approx 80 \text{ GPa}$. The post-shock pressure at $x \approx 1700$ obtained in the bottom right panel of Fig. 2 is in agreement with this estimate. The shock wave heats the ions. The ion temperature in the postshock region of a strong shock wave with compression ratio equal to $\kappa = (\gamma + 1)/(\gamma - 1)$ is for our application approximately [9]:

$$k_B T_i = A m_p v^2 \frac{1 - 1/\kappa}{\kappa}, \quad (1)$$

where k_B , m_p and A are the Boltzmann constant, the proton mass and atomic mass, respectively. For xenon with atomic mass $A = 131$, a shock velocity of 110 km/s , and an adiabatic index of $\gamma = 5/3$ for ions gives a postshock temperature of $T_i \approx 3 \text{ keV}$. We find with the numerical simulation an ion temperature of 1.2 keV in Fig. 3 that shows the region around the shock. With an effective resolution of $1.6 \mu\text{m}$ we do not fully resolve this narrow ion temperature peak, resulting in a lower than expected maximum temperature. We find two other temperature peaks as well. One peak is near $x = 1600 \mu\text{m}$ behind the shock and another is near $y = 250 \mu\text{m}$. They overlap with the beryllium-xenon and the polyimide-xenon material interfaces, respectively. These spikes are probably the result of a low-order convergence rate in the interface treatment.

For a high density plasma the collision frequency between electrons and ions is large, so that their temperature will equilibrate. At the shock, however, the ion temperature jumps so that the ions and electrons are out of equilibrium. The ions will heat the electrons via Coulomb collisions and form an equilibration zone directly behind the shock. The

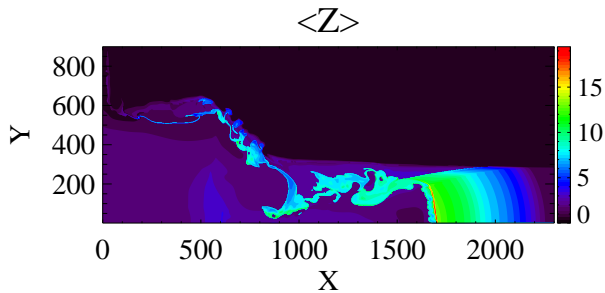


Figure 4: The mean ionization in the circular nozzle simulation as a function of the x and y coordinates in microns.

electron heating will also increase the ionization in the equilibration zone. Fig. 4 shows the average ionization in the xy -plane. We find from the code that the ionization is elevated to about $\langle Z \rangle = 17$ at the electron temperature peak in the equilibration zone. At this peak the energy of each ion is shared with $\langle Z \rangle$ electrons. The equilibration temperature T_{eq} can be approximated as the postshock temperature for a strong shock under the assumption that the electrons and ions are in temperature equilibrium:

$$k_B T_{\text{eq}} = \frac{1}{\langle Z \rangle + 1} A m_p v^2 \frac{1 - 1/\kappa}{\kappa}. \quad (2)$$

For representative values of the polytropic index between $\gamma = 1.2$ and 1.3 for single-temperature xenon, the estimated equilibration temperature is between $T_{\text{eq}} = 76$ eV and 104 eV. In reality this temperature will be somewhat lower due to radiative cooling. The numerically obtained value is $T_e \approx 73$ eV in Fig. 2. This electron temperature is not the final state in the postshock region since $\sigma T_e^4 \approx 2.8 \times 10^{12}$ W/cm², where σ is the Stefan–Boltzmann constant. The incoming kinetic energy flux is however $\rho v^3/2 \approx 4.3 \times 10^{11}$ W/cm² based on the velocity at time $t = 13$ ns of $v = 110$ km/s and xenon density $\rho = 0.0065$ g/cm³. There is therefore not enough incoming energy. There must be a cooling layer [1] through which the electron temperature falls to the final temperature T_f estimated by $2\sigma T_f^4 = \rho v^3/2 \approx 4.3 \times 10^{11}$ W/cm². The factor 2 is because the radiative cooling layer emits in both directions equally. The final temperature is thus $T_f \approx 38$ eV.

The heated electrons are the main energy source for radiation. In Fig. 2 we show the radiation temperature as a measure for the total radiation energy density. The photons travel upstream of the shock where they preheat and ionize the unshocked xenon in the precursor as depicted in the electron temperature panel in Fig. 2 and Fig. 4. The radiation transport in the unshocked xenon is not diffusive and we rely on the flux-limited diffusion to recover the optically thin free-streaming limit. This free-streaming approximation is accurate enough as long as the radiation transport from the precursor back to the shock is negligible, in contrast with the almost omnidirectional photon distribution function as assumed in the diffusive limit. A fraction of the upstream radiation expands sideways and heats the polyimide wall ahead of the primary shock. This will ablate the polyimide of the wall. The resulting inward polyimide flow is visible in the Y velocity panel of Fig. 2. This infow extends at 13 ns to $x \approx 2100$ μm and does have a magnitude of about 10 km/s. The exact magnitude of this flow might depend on the radiation transport fidelity used in simulations. The ablated polyimide compresses the xenon as can be seen in the density panel in Fig. 2 by the faint tilted feature between $x \approx 1700$ μm and $x \approx 2100$ μm . The resulting wall shock has an angle with the primary shock and their shock properties were analyzed in [2, 3].

The material identity in the top left panel of Fig. 2 also demonstrates the entrainment of xenon in between the beryllium and polyimide. In [3] the entrained flow was shown to first get shocked by the wall shock and then again shocked near the tripple point of the wall shock and the primary shock. We also mention that in our simulations the entrained shear flows produce Kelvin–Helmholtz roll-ups at for instance $x \approx 1400$ μm .

The simulation presented in this section was performed in 3D Cartesian geometry. The axi-symmetry in the problem does however allow to perform this simulation in 2D cylindrical rz -geometry as well. We used the same settings for the numerical radiation-hydrodynamics solvers. The computational domain is $-150 < z < 3900$ and $0 < r < 900$ in microns, where r is the radial coordinate and z is now the coordinate along the tube. The effective resolution is 2560×512 using two levels of refinement, so that the cell sizes in the rz -geometry correspond to the cell sizes in the xy -plane in the 3D Cartesian simulation. The 2D mesh is decomposed in 4×4 grid blocks. The mesh

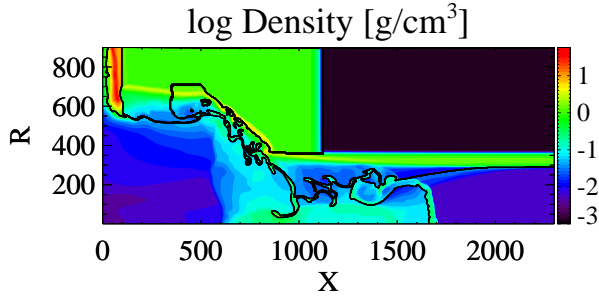


Figure 5: The density at 13 ns in color contour. This simulation is performed in the rz -geometry. The axes are in microns and the black line indicates the change in material level.

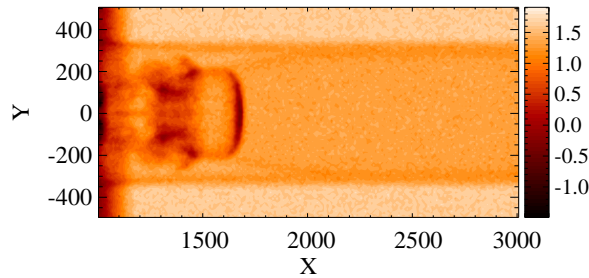


Figure 6: Synthetic radiograph image at 13 ns for the circular nozzle simulation. The X-ray source is located at $(x, y, z) = (2, -12, 0)$ in mm.

refinement criteria are also the same as for the 3D case. In Fig. 5 the density is shown at the final time 13 ns. The results are quite similar to those of the previous simulation. The main difference is in the entrained xenon, which requires probably higher resolution to be fully resolved.

The aim of the CRASH project is to predict certain properties of the compound shock in our high-energy-density laser experiments. From the experiment we obtain X-ray radiograph images using He- α emission from a backlit pinhole source transmitting through the experimental target. These images show fundamentally where the dense xenon is. To be able to make a direct comparison between the observations and simulations, we added the capability to the CRASH code to create synthetic radiograph images. The details of the implementation and verification are presented in Appendix B. The radiograph for the circular nozzle simulation is shown in Fig. 6. We locate the X-ray source at $(x, y, z) = (2000, -12000, 0)$ μm . We have blurred the image to account for the finite pinhole size and finite exposure time in the experiment. We also added Poisson noise to mimic the finite photon count. The dense xenon behind the primary shock at $x = 1700$ μm and the wall shock is clearly visible. We can also see the entrained xenon and the Kelvin-Helmholtz roll-up to the left of the primary shock.

3. Elliptical nozzle

The setup of the elliptical nozzle is very similar to that of the circular nozzle. The main difference is that the wide tube of 1200 μm inner radius changes the cross-section down the tube into an ellipse with a major axis of 1200 μm and a minor axis of 600 μm . The first 1.1 ns of the simulation is, as for the circular nozzle, performed with the H2D radiation-hydrodynamics code to determine the laser energy deposition. For the tube geometry in H2D a straight tube is used with a diameter of 1200 μm . The output of H2D is used to initialize the CRASH code following the recipe outlined in Appendix A. If we use the notation that x is the coordinate along the tube and y and z are the two directions transverse to the tube, then we remap the straight tube of H2D to CRASH using the coordinate transformations shown by the equations A.4 and A.5 in which $x_0 = 500$ μm , $x_1 = 750$ μm , $\varepsilon_y = 1/2$ and $\varepsilon_z = 1$. That means that the circular

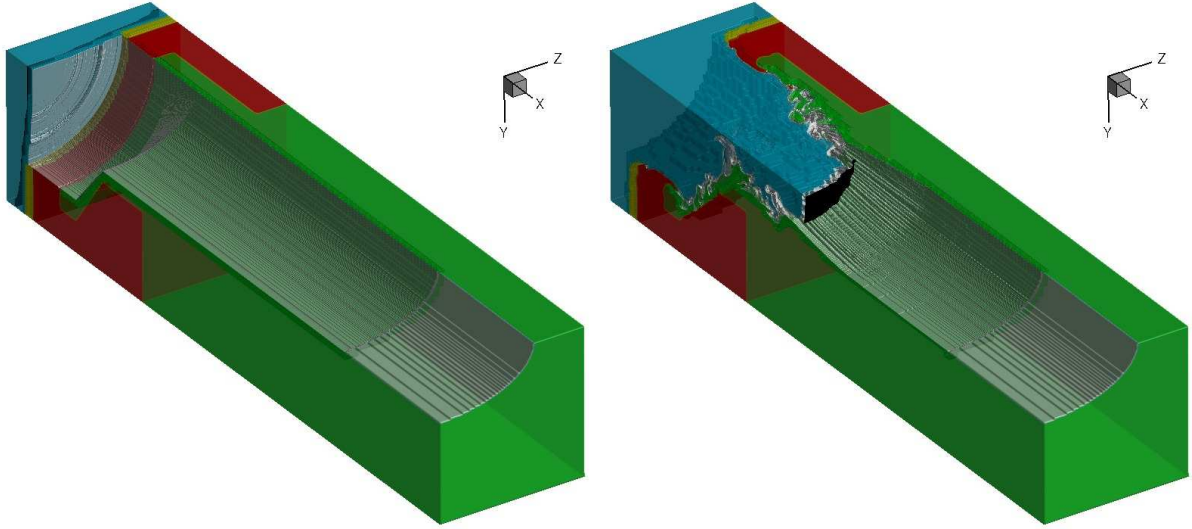


Figure 7: The materials in the 3D elliptical nozzle simulation at 1.1 ns (left panel) and 13 ns (right panel). One quarter of the nozzle is shown. The color code for the materials is the same as in 1. The black iso-surface indicate the primary shock.

tube is tapered into an elliptical shaft between $x_0 = 500 \mu\text{m}$ and $x_1 = 750 \mu\text{m}$. The domain size, effective resolution, refinement criteria, boundary conditions, and the used numerical scheme are the same as for the circular nozzle.

The simulation is performed from 1.1 ns to 13 ns physical time. The number of finite volume cells increased from 29.6 million initially to about 45.3 million at the end of the simulation. The computational time was 3.5 days on 1000 processor cores of the HERA supercomputer. The 3D material identification is shown in Fig. 7. The left panel is for 1.1 ns and the right panel for 13 ns. The color code is blue for beryllium, green for polyimide, red for acrylic and yellow for gold. Xenon is for convenience not colored in these panels so that the elliptical shaft is visible. At 13 ns the beryllium has moved into this shaft and drives a shock in the xenon like a piston. The shock front is indicated with a black surface. The edge of the volume occupied by the xenon is colored in white to visualize the entrainment of xenon between the polyimide and beryllium.

The left panels of Fig. 8 show the material location, mass density and electron temperature, respectively, in the xz -plane at 13 ns. The basic ingredients of the compound radiative shock structure are seen in these panels. The primary shock near $x \approx 1700 \mu\text{m}$ in this plane is curved, since the diameter of the laser spot of $800 \mu\text{m}$ is smaller than the major axis, $1200 \mu\text{m}$, of the elliptical shaft. The ripple in the compressed xenon region behind the primary shock was analyzed for similar experimental conditions [10]. We also find again the tilted wall shock in front of the primary shock. The electron temperature panel shows the temperature peak in the equilibration zone behind the primary shock and a decreasing temperature behind that in the radiative cooling zone. The right panels of Fig. 8 show the same physical quantities in the vertical yz -plane. The shock structure in this plane is quite similar to the results found for the circular nozzle.

The difference in the shock structure and compressed xenon region behind the shock should also be visible in the synthetic radiographs. Indeed, in Fig. 9 we show in the left panel the image produced by an X-ray source at $(x, y, z) = (2000, -12000, 0) \mu\text{m}$ directed at the xz -plane and in the right panel the image produced by an X-ray source at $(x, y, z) = (2000, 0, 12000) \mu\text{m}$ directed at the xy -plane. The compressed xenon behind the primary and wall shock are found as dark features in these images. Note that the image in the right panel is darker than the image in the left panel, since the rays are going through twice as much xenon (the major axis is twice the minor axis). Also note that the rippled structure of the compressed xenon layer behind the primary shock is somewhat smoothed out in these images.

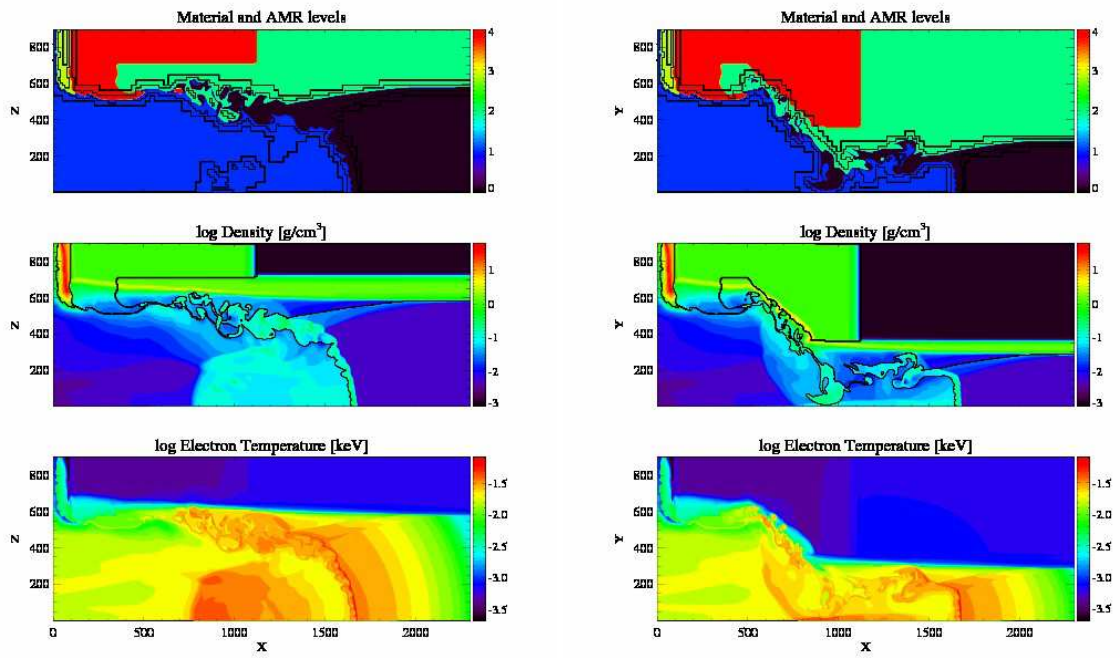


Figure 8: The output of the 3D elliptical nozzle simulation at 13 ns. The state variables indicated in the plot titles are shown in color as a function of the (x, z) coordinates given in microns in the $y = 0$ plane on the left and (x, y) coordinates in the $z = 0$ plane on the right. The color bars provide the scales. The color code of the material levels in the top panels indicates the same materials as in Fig. 2. The black lines in the top panels are for the resolution changes, while the black lines in the middle panels indicate the change in material identity.

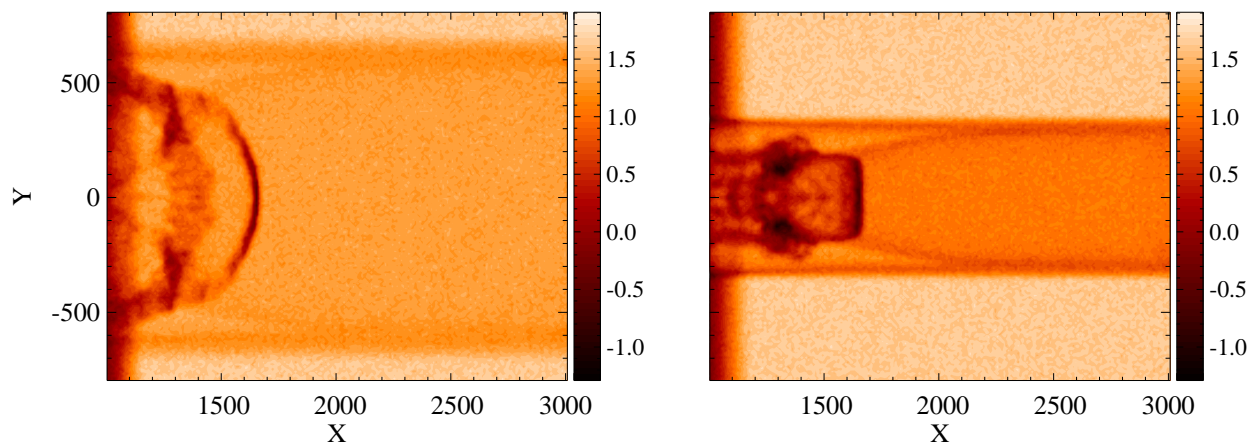


Figure 9: Synthetic radiographs created along the two transverse axes of the 3D elliptic nozzle at 13 ns. The X-ray sources are at $(x, y, z) = (2, -12, 0)$ mm directed at the $y = 0$ (left panel) and at $(x, y, z) = (2, 0, 12)$ mm directed at the $z = 0$ plane (right panel).

4. Conclusions

In this paper we have discussed the simulations of radiative shocks in nozzle shaped tubes. We recover basic properties found in laser-driven shock experiments in high-energy-density facilities and from radiation hydrodynamic theories: A compressed layer shows up directly behind the primary shock in which the electrons are heated in an equilibration zone by the shock wave heated ions. This is followed by a radiative cooling layer. The emitted photons propagate upstream and preheat the precursor ahead of the primary shock. The lateral expansion of this radiation ablates the plastic nozzle which results in a wall shock. The simulations are shown to be in agreement with simple back-of-the-envelope estimates.

We have used the two-dimensional version of the Hyades code to determine the laser energy deposition during the first 1.1 ns of the experiment. This code simulates on a Lagrangian mesh the radiation hydrodynamics based on a multi-group flux-limited diffusion model and flux-limited electron thermal heat conduction. We are currently constructing a laser package in the Eulerian CRASH code so that the laser energy deposition and the produced radiative shocks in the xenon at later times are self-consistently evaluated with the same code.

We plan to perform laser-driven shock experiments in three-dimensional circular and elliptical nozzles. The comparison of the elliptical nozzle simulations with such experiments will stress test the performance of the code. For the validation we can compare the properties of the shock structure and compressed xenon layers from both the simulations and experiments. These 3D properties can in the experiments be extracted from dual, orthogonal radiography [11] and then compared to the two orthogonal synthetic radiographs from the simulations.

Acknowledgments

This work was funded by the Predictive Sciences Academic Alliances Program in DOE/NNSA-ASC via grant DEFC52-08NA28616 and by the University of Michigan. The authors acknowledge M.J. Grosskopf and E. Rutter for providing Hyades simulations. The authors would also like to thank B. Fryxell and E. Myra for helping to test the CRASH code.

Appendix A. Initializing CRASH with Hyades

The laser energy deposition during the first 1.1 ns is evaluated with the Lagrangian radiation hydrodynamics code Hyades 2D (H2D) [4]. The output of H2D is on a distorted logically Cartesian mesh of $n_x \times n_y$ cells. When we initialize the CRASH code with H2D, this mesh is first triangulated by splitting each quadrilateral along the shorter diagonal. The interpolation from the triangulated Hyades grid requires finding the triangle that surrounds the center of a given grid cell of the CRASH code. A simple linear search can become very inefficient when we have many grid cells (order of a hundred thousand) per processor. To accelerate this method, first we create a uniform grid with about 200 by 200 resolution that covers the whole domain. For each rectangular cell in the uniform grid we find and store the list of triangles that intersect it. This can be done very fast. Then we perform the interpolation onto the CRASH grid by first finding the rectangular cell that surrounds it, and then we only check the triangles that intersect this cell to see which one contains the CRASH grid cell center.

The H2D simulations are performed on a Lagrangian grid where all cells correspond to a unique material. These materials are identified by a material index in the H2D output. Our code uses an Eulerian grid and we track the material by means of level set functions. These level set functions are smooth and signed distance functions, initialized with the following algorithm. For each cell i of the H2D grid having material index α_i , the level set function for material α_i is set to the distance to the closest H2D cell that contains a material different from α_i :

$$d_{\alpha_i}(i) = + \min_{j, \alpha_j \neq \alpha_i} |\mathbf{r}_i - \mathbf{r}_j|, \quad (\text{A.1})$$

where \mathbf{r}_i is the location of cell i . The level set functions for the other materials, $\beta \neq \alpha_i$, are set to the negative distance to the closest cell containing material β :

$$d_{\beta}(i) = - \min_{j, \alpha_j = \beta} |\mathbf{r}_i - \mathbf{r}_j|. \quad (\text{A.2})$$

We interpolate these level set functions to the cells on the CRASH grid. In our first-order level set scheme the material in the cell is indicated by the largest level set function. For the simulations with H2D of our shock tube experiments we use xenon, beryllium, polyimide, gold, acrylic and “vacuum”. In CRASH, vacuum is reassigned as polyimide with low mass density. At later times during the evolution, the location of material m follows the simple advection equation for the level set function

$$\frac{\partial d_m}{\partial t} + \nabla \cdot (d_m \mathbf{u}) = d_m \nabla \cdot \mathbf{u}. \quad (\text{A.3})$$

Also here, the material having the largest d_m is assigned to be the material of the cell.

A 3D nozzle is created from 2D Hyades as follows. We first read the H2D shock tube output and triangulate the data. After that we transform the coordinates in the transverse directions y and z . The circular cross section of the tube shrinks into an ellipse or smaller circle by means of

$$y' = y \left[1 + (\varepsilon_y - 1) \max \left(0, \min \left(1, \frac{x - x_0}{x_1 - x_0} \right) \right) \right], \quad (\text{A.4})$$

$$z' = z \left[1 + (\varepsilon_z - 1) \max \left(0, \min \left(1, \frac{x - x_0}{x_1 - x_0} \right) \right) \right], \quad (\text{A.5})$$

where ε_y and ε_z are the factors with which the y and z coordinates contracts for $x > x_1$ along the tube. This shrinking varies linearly between x_0 and x_1 . For $x < x_0$ the tube is not modified. This means that the plasma at the far end is relocated closer towards the axis. This will change the output of H2D to an unphysical state (the solution of the straight tube is not the same as the solution of the nozzle). The impact of this change in geometry is however minimal since at 1.1 ns the shock dynamics did not yet reach the far end of the shock tube.

Appendix B. Synthetic radiographs

The CRASH code has the capability of generating synthetic radiographs during the simulations. The time frequency of the plotting, the location (or possible locations) of the X-ray source(s) and the orientation, size, and number of pixels of the radiograph images are all input parameters.

In the CRASH shock tube experiments we typically produce radiographs by transmitting 5.18 keV (mainly V He-alpha line) X-rays through material whose temperature is of the order of 50 eV. These X-rays interact only weakly with the free or outer electrons. We can therefore use cold opacities for the materials in the experiment to evaluate the transmission. X-ray photons at this energy experience negligible refraction in the experimental target. So it is legitimate for our radiograph calculation to use straight-line analysis.

These images are line-of-sight plots that calculate the optical depth along the straight lines (rays), connecting the X-ray source to the center of the image pixel. The optical depth is an integral of the mass density multiplied by the specific opacity characteristic for the material and the spectrum of the X-ray source along the ray:

$$D = \int_0^\infty \rho(\mathbf{r}(l)) \kappa(\mathbf{r}(l)) dl, \quad (\text{B.1})$$

where κ is the specific opacity of the materials used in the experiments and the ray is parameterized by the distance l to the source. In our shock-tube experiments [8], we assume that the absorption is dominated by the X-ray line near 5.18 keV and the specific opacities of the commonly used materials are 79.4, 0.36 and 2.24 m²/kg for xenon, beryllium and polyimide, respectively. In our experiments we also use acrylic and gold, but these materials are outside the view of the radiograph, so that we do not need their specific opacity values accurately. For acrylic we use the same value as for polyimide and we use the large value 10¹⁰ m²/kg for gold.

The parallel algorithm is implemented in the following way: For each ray and each grid block we determine first the segment of the ray if it intersects the block. Then we integrate for each ray and block the optical depth B.1 using a trapezoidal rule and a tri-linear interpolation. The step size of the integration is proportional to the cell size of the block. Once the integration is done for all blocks, we add up for each ray all integrals over the block segments using a call to MPI_reduce. For the rz -geometry we consider the 2D blocks as rings in 3D with rectangular cross-section. The integration along the ray segments is performed in 3D, but we use a bi-linear interpolation to obtain $\rho\kappa$ at the required integration points.

We have verified the implementation with an analytical problem where we integrate along rays through a 3D sphere of a given density profile and specific opacity of value one. The density inside the sphere of radius R is defined as $\rho = R^2 - r^2$ if the radial distance from the center of the sphere is $r \leq R$, while $\rho = 0$ for $r > R$. The density can be integrated analytically along a ray passing through this sphere at a distance δ from the center. The total length of the segment of this ray inside the sphere is $2S = 2\sqrt{R^2 - \delta^2}$. With these definitions, the optical depth B.1 along this line segment becomes

$$D = \int_{-\infty}^{\infty} \rho(s) ds = \int_{-S}^S (R^2 - \delta^2 - s^2) ds = \frac{4}{3}(R^2 - \delta^2)^{3/2}, \quad (\text{B.2})$$

where s is the coordinate along the ray such that $|s| = \sqrt{r^2 - \delta^2}$ is the distance to the middle of the line segment. The radiograph image is always a plane through the origin. A pixel with coordinates (x', y') of this image is then at a distance $d = \sqrt{x'^2 + y'^2}$ from the origin (here and in the following the prime indicates the coordinate system associated with the radiograph image). The location of the X-ray source is assumed to be on the z' -axis at a distance L from the center of the sphere. The ray connecting this source and the pixel (x', y') will then have a minimum distance to the center of the sphere of $\delta = dL / \sqrt{L^2 + d^2}$, as can be deduced from similar triangles. The final formula for the optical depth along this ray now becomes

$$D = \max\left(0, \frac{4}{3} \left[R^2 - \frac{L^2}{1 + L^2/(x'^2 + y'^2)} \right]^{3/2}\right). \quad (\text{B.3})$$

In the verification test we place the X-ray source at $(x, y, z) = (60, 80, 100)$ and the radiograph image is always orthogonal to the line connecting the source and center of the sphere, so that the distance between the source and image is $L = 100\sqrt{2}$. The density sphere has a radius $R = 10$. The left panel in Fig. B.10 shows the simulated image for a grid resolution of 40^3 cells at the base level and one level of refinement for $y > 0, z > 0$. The right panel shows the difference relative to the analytical formula B.3. Note that the error is smaller where the rays go through the refined region of the grid. The grid convergence is seen in Fig. B.11 for three different resolution at the base level: $20^3, 40^3$, and 80^3 . The relative error is calculated from

$$E_{L1} = \frac{\sum_{i=1}^I |D_i - D_{\text{ref}i}|}{\sum_{i=1}^I |D_{\text{ref}i}|}, \quad (\text{B.4})$$

where D is the simulated optical depth, D_{ref} is the analytical reference B.3 and $i = 1, \dots, I$ indexes the pixels of the image. We obtain second-order convergence. We have also verified the implementation for the rz -geometry, in which case the sphere is a circle rotated around the symmetry axis.

The simulated radiographs can be compared with experimental backlit pinhole radiographs for validation studies. To make these images appear more similar, we need to take into account the finite pinhole size of about 20 mm diameter, the finite exposure time of about 0.2 ns and the effect of a finite number of collected photons (typically 50 photons per 100 nm^2 image pixel). The first two effects are approximated by smoothing the synthetic radiograph over a few pixels. The finite photon count can be taken into account by using

$$D' = -\ln[P(50)e^{-D}] = D - \ln P(50), \quad (\text{B.5})$$

instead of D , where $P(50)$ is a random number with a Poisson distribution and a mean value of 50. The second equality shows that this is the same as subtracting the logarithm of these random numbers from the original simulated radiograph during the post-processing step. In Fig. B.12 the original synthetic radiograph is compared with the post-processed image.

Appendix C. Improved diffusion operator at resolution changes

In this appendix we present an improved conservative and spatially second-order implicit scheme for the radiation diffusion and heat conduction. For convenience, we only derive this scheme for the heat conduction. The generalization for radiation diffusion is straightforward.

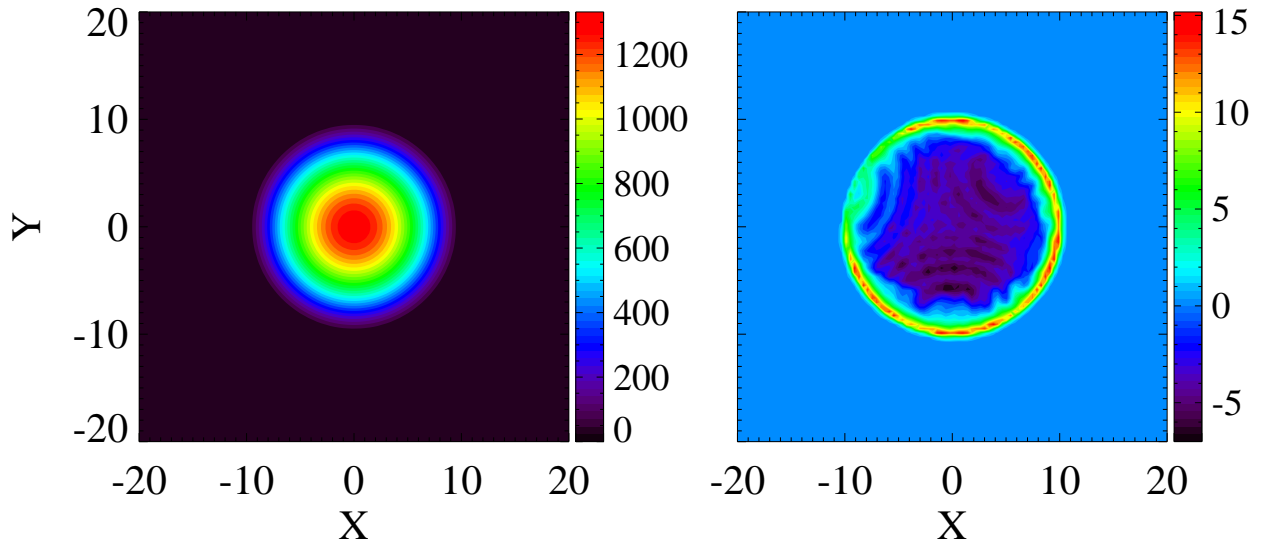


Figure B.10: The radiograph image for an analytical density sphere on a non-uniform mesh and a specific opacity with value one. The X-ray source is located at $(x, y, z) = (60, 80, 100)$. The left panel shows the simulated image, while the right panel is for the error relative to the analytical solution.

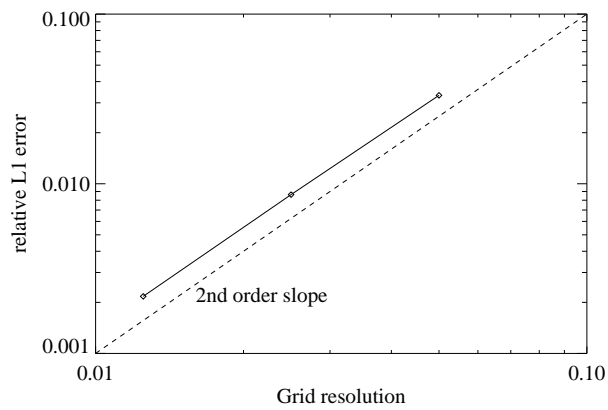


Figure B.11: The L1 error of the optical depth relative to the analytical reference for 20^3 , 40^3 and 80^3 base resolutions and one level of refinement for $x > 0$, $y > 0$ and $z > 0$.

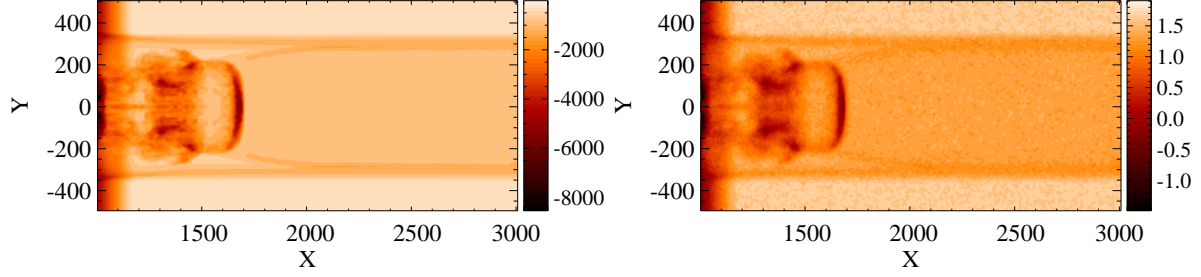


Figure B.12: Original synthetic radiograph (left panel) and the processed image after smoothing and adding Poisson noise to mimic the experimental radiograph (right panel).

Discretizing the electron thermal heat conduction implicitly in time leads to the linearized backward Euler equation for the electron temperature T

$$C_{Ve}^* \frac{T^{n+1} - T^*}{\Delta t} = \nabla \cdot C_e^* \nabla T^{n+1}, \quad (\text{C.1})$$

where C_{Ve} is the electron specific heat and C_e is the heat conduction coefficient. The time level $*$ corresponds to the state before the implicit update. During the implicit advance with time step Δt , the coefficients are frozen in at time level $*$, resulting in a temporally first order scheme in general. This equation can be recast in a linearized equation for the change $\Delta T = T^{n+1} - T^*$:

$$\left[\frac{C_{Ve}^*}{\Delta t} - \nabla \cdot C_e^* \nabla \right] \Delta T = \nabla \cdot C_e^* \nabla T^*. \quad (\text{C.2})$$

The right-hand-side depends only on time level $*$. Once Eq. C.2 is solved using a linear solver, the electron energy density can be updated using

$$E_e^{n+1} = E_e^* + C_{Ve}^* (T^{n+1} - T^*), \quad (\text{C.3})$$

to conserve the energy.

A discrete set of equations is obtained by applying a finite volume method to Eq. C.2. To make this scheme spatially second-order accurate on a uniform mesh, we need a second order accurate thermal heat flux at the face centers. This is achieved by approximating the gradient of the electron temperature with a central difference using the cell-centered values

$$-\int_{V_i} \nabla \cdot (C_e \nabla T) dV = \sum_j S_{ij} C_{ej} \frac{T_i - T_j}{|\mathbf{x}_i - \mathbf{x}_j|}, \quad (\text{C.4})$$

where the control volumes are indexed by i , each having a volume V_i . The index j is for the neighboring cells having a common interface with area S_{ij} and a distance between the cell centers is $|\mathbf{x}_i - \mathbf{x}_j|$. The heat conduction coefficient at the face is the arithmetic average of the coefficient at the two neighboring cell centers, $C_{ej} = (C_{ei} + C_{ej})/2$.

To obtain a second-order heat flux at the resolution change, we need a third-order interpolation of the temperature in the ghost cells. Such an interpolation was previously used in the context of Hall magnetohydrodynamics (MHD) [12]. This interpolation is only needed for the fine cells, since the flux at the coarse side will be obtained as the sum of the fluxes at the neighboring fine cells to preserve conservation of the scheme [13]. The implementation for the heat conduction is different from the Hall MHD, since for the heat conduction we also have to maintain positivity of the temperature and avoid spurious oscillations. For convenience we will restrict the analysis to two-dimensional domains. The third-order interpolation for the temperature value at the fine ghost cell $(0, j)$, indicated by the dashed circle, is first performed along the coarse cell values in the transverse direction to obtain the temperature at $(-1/2, j)$ as depicted in Fig. C.13:

$$T_{-1/2,j} = \frac{5T_{-1/2,j-3/2} + 30T_{-1/2,j+1/2} - 3T_{-1/2,j+5/2}}{32}. \quad (\text{C.5})$$

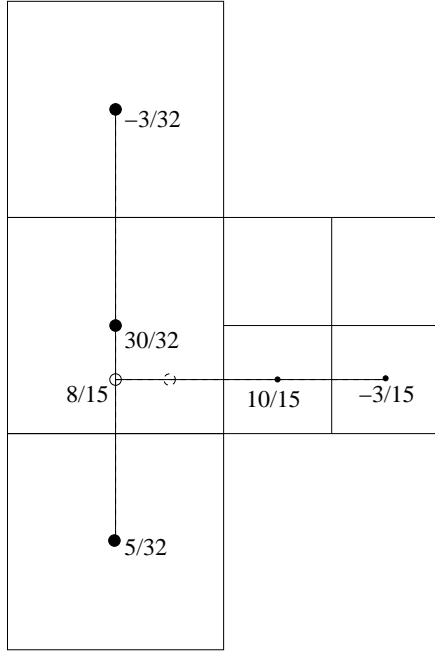


Figure C.13: The coefficients of the third-order interpolation near the resolution changes (similar to [12]). The order of the interpolation is first along the coarse grid cells tangential to the resolution change, followed by an interpolation along the fine cells to obtain a third-order temperature value in the fine ghost cell indicated by the dashed circle.

To guarantee the positivity of the interpolated temperature, the value is clipped by the maximum and minimum values of the surrounding points

$$T_{-1/2,j} = \max\{\min[T_{-1/2,j}, \max(T_{-1/2,j-3/2}, T_{-1/2,j+1/2})], \quad (C.6)$$

$$\min(T_{-1/2,j-3/2}, T_{-1/2,j+1/2})\}. \quad (C.7)$$

The value in the fine ghost cell can now be obtained by a parabolic interpolation along the fine cells in the direction normal to the refinement interface

$$T_{0,j} = \frac{8T_{-1/2,j} + 10T_{1,j} - 3T_{2,j}}{15}. \quad (C.8)$$

For this interpolation we need again to clip the obtained value with the surrounding temperatures

$$T_{0,j} = \max\{\min[T_{0,j}, \max(T_{-1/2,j}, T_{1,j})], \min(T_{-1/2,j}, T_{1,j})\}. \quad (C.9)$$

This ghost cell value is used in the heat conduction formula C.4. We still need a second order accurate heat conduction coefficient C_{ej} at the fine face center. This amounts to a second-order prolongation of the heat conduction coefficient to obtain the ghost-cell values at the fine side, followed by an averaging of the cell centered coefficients to the face center. Once the thermal heat fluxes at the fine side are obtained, conservation is restored by copying the fine fluxes to the coarse side at the resolution changes. Note that this scheme is different from [14] where conservation of the flux at the resolution changes is enforced in the strong sense by enforcing the flux on the coarse side to be equal to each of the fluxes on the fine side.

In the analysis we assumed a Cartesian mesh. Generalization to curvilinear grids is presented in [12]. The same third-order interpolation procedure with clipping is also used for heat conduction along the magnetic field lines in the context of solar wind modeling [15].

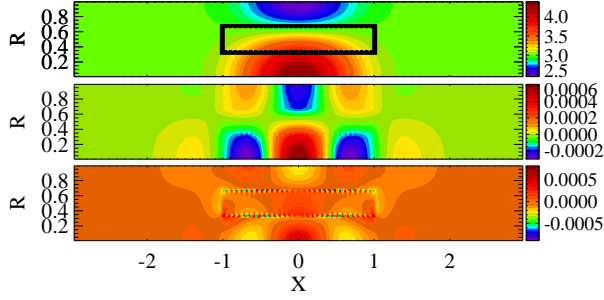


Figure C.14: Heat conduction test in rz -geometry with uniform coefficients. The top panel shows the electron temperature in color contour at the final time $t = 3/2$. The resolution changes are indicated by the black box. The middle panel is for the temperature error relative to the reference solution, while the bottom panel shows the relative error of the original heat conduction scheme [5].

To verify that the improved implicit heat conduction and radiation solver is second order, we first demonstrate a uniform heat conduction test in rz -geometry. This test follows the time evolution of the electron temperature profile for a purely heat conductive plasma similar as described in [5]. We set the electron specific heat to be one and further assume the heat conductivity C_e to be a constant. The time evolution for this problem is a product of a Gaussian profile in the z -direction and the Bessel function J_0 in the r -direction:

$$T = T_{\min} + T_0 \frac{1}{\sqrt{4\pi C_e t}} e^{-\frac{z^2}{4C_e t}} J_0(br) e^{-b^2 C_e t}, \quad (\text{C.10})$$

where $b \approx 3.8317$, $T_{\min} = 3$, $T_0 = 10$, and $C_e = 0.1$.

The domain size for this problem is $-3 < z < 3$ and $0 < r < 1$, which we decompose in 3×3 grid blocks of 30×30 cells each. The central block, $-1 < z < 1$ and $1/3 < r < 2/3$, is mesh refined by one level. At the outer boundary we fix the ghost cells to the exact solution C.10, except for $r = 0$, in which case we apply a symmetry condition. We simulate the time evolution from $t = 1$ to $t = 3/2$ using the GMRES iterative solver with a Schwarz-type ILU preconditioner. To achieve second-order time integration we use the Crank-Nicolson approach. The latter is possible since the coefficients in the problem are all temporally invariant.

The final solution with 90^2 base resolution is shown in the top panel of Fig. C.14. The color is for the electron temperature. The change in the grid resolution with one level of refinement is indicated by the black line. To demonstrate that the temperature error at these resolution changes is not significantly larger than at the uniform part of the mesh, we also plot the spatial distribution of the temperature error in the bottom panel. The maximum error is clearly at the coarse grid away from the resolution changes.

We use the relative maximum error to study the grid convergence. This error is defined by

$$E_{L_\infty} = \frac{\max_{i=1,\dots,I} |T_i - T_{\text{ref}_i}|}{\max_{i=1,\dots,I} |T_{\text{ref}_i}|}, \quad (\text{C.11})$$

in which T is the numerical solution on the $i = 1, \dots, I$ control volumes and T_{ref} is the analytical reference in Eq. C.10. The second-order convergence rate is depicted in Fig. C.15 for grid resolutions of 90^2 , 180^2 , 360^2 , and 720^2 at the base level.

To demonstrate that the new heat conduction and radiation solver does not under- or over-shoot near discontinuities, we show the Mach 5 non-equilibrium gray-diffusion test of [16]. This test uses non-uniform radiation diffusion coefficient and Planck opacity that depend on the density and temperature as defined by $D_r = 0.0175(\gamma T)^{7/2}/\rho$ and $c\kappa_P = 10^6/D_r$. In [5], this verification was transformed to a heat conduction test. Here, we will keep it as a radiation test. We add a Mach -5 flow to the 1D initial condition, so that both the shock and radiation condition will move to the left with a Mach -5 velocity. This solution is then rotated counter-clockwise over an angle $\tan^{-1}(1/2)$ on a 2D grid to make the test problem more difficult. The domain size is $-0.0384 < x < 0.0384$ by $-0.0048 < y < 0.0048$ and within the region $-0.0128 < x < 0.0128$ and $-0.0016 < y < 0.0016$ we refine the mesh by one level. The grid is designed in

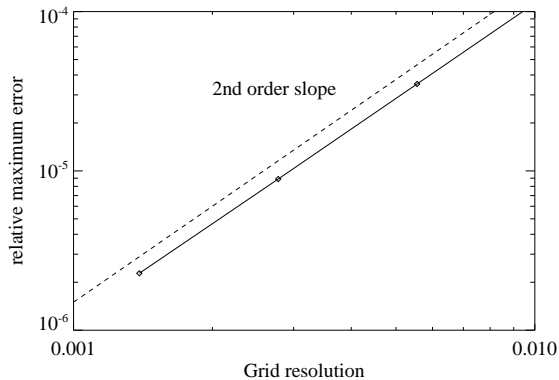


Figure C.15: Relative maximum error for the heat conduction test in rz -geometry and with uniform coefficients. Second-order convergence is achieved on a non-uniform grid.

such a way that during the time evolution both the shock and the radiation precursor front travel through a resolution change. For the simulation of the hydrodynamic part, we use the HLLC scheme with the generalized Koren limiter by setting $\beta = 3/2$ and a CFL of 0.8. The radiation diffusion and energy exchange between the radiation and material are solved implicitly with the new implicit method using the GMRES iterative solver with a block ILU preconditioner.

The material and radiation temperatures at the final time, $t = 0.0025$, are shown in the left and right panel of Fig. C.16, respectively. The solid, dotted, dashed, and dot-dashed black lines indicate the base resolutions of 192×24 , 384×48 , 768×96 , and 1536×192 , respectively. The blue line is the semi-analytic solution of [16]. The new scheme correctly solves the precursor front at $x \approx -0.022$ and shock front at $x \approx 0.0085$ without spurious oscillations.

References

- [1] A.B. Reighard, R.P. Drake, The formation of a cooling layer in a partially optically thick shock, *Astrophys. Space Sci.* 307 (2007) 121–125.
- [2] F.W. Doss, H.F. Robey, R.P. Drake, C.C. Kuranz, Wall shocks in high-energy-density shock tube experiments, *Phys. Plasmas* 16 (2009) 112705
- [3] F.W. Doss, R.P. Drake, E.S. Myra, Oblique radiative shocks, including their interactions with non-radiative polytropic shocks, *Physics of Plasmas* 18 (2011) 056901.
- [4] J.T. Larsen, S.M. Lane, Hyades: a plasma hydrodynamics code for dense plasma studies, *J. Quant. Spectrosc. Radiat. Transf.* 51 (1994) 179–186.
- [5] B. van der Holst, G. Tóth, I.V. Sokolov, K.G. Powell, J.P. Holloway, E.S. Myra, Q. Stout, M.L. Adams, J.E. Morel, S. Karni, B. Fryxell, R.P. Drake, A block-adaptive-mesh code for radiative shock hydrodynamics: Implementation and verification, *Astrophys. J. Suppl.* 194 (2011) 23.
- [6] G. Tóth, B. van der Holst, I.V. Sokolov, D.L. De Zeeuw, T.I. Gombosi, F. Fang, W.B. Manchester, X. Meng, D. Najib, K.G. Powell, Q.F. Stout, A. Gloer, Y.-J. Ma, and M. Opher, Adaptive Numerical Algorithms in Space Weather Modeling, *J. Comp. Phys.* (2011) doi:10.1016/j.jcp.2011.02.006.
- [7] J.P. Holloway, D. Bingham, C. Chou, F. Doss, R.P. Drake, B. Fryxell, M. Grosskopf, B. van der Holst, R. McClarren, A. Mukherjee, V. Nair, K.G. Powell, D. Ryu, I. Sokolov, G. Tóth, and Z. Zhang, Predictive Modeling of a Radiative Shock System, *Reliability Engineering and System Safety* (2011) doi:10.1016/j.res.2010.08.011.
- [8] R.P. Drake, F.W. Doss, R.G. McClarren, M.L. Adams, N. Amato, D. Bingham, C.C. Chou, C. DiStefano, K. Fidkowski, B. Fryxell, T.I. Gombosi, M.J. Grosskopf, J.P. Holloway, B. van der Holst, C.M. Huntington, S. Karni, C.M. Krauland, C.C. Kuranz, E. Larsen, B. van Leer, B. Mallick, D. Marion, W. Martin, J.E. Morel, E.S. Myra, V. Nair, K.G. Powell, L. Raushberger, P. Roe, E. Rutter, I.V. Sokolov, Q. Stout, B.R. Torralva, G. Tóth, K. Thornton, A.J. Visco, Radiative Effects in Radiative Shocks in Shock Tubes, *High Energy Density Phys.* 7 (2011) 130.
- [9] R.P. Drake, *High Energy Density Physics: Fundamentals, Inertial Fusion and Experimental Astrophysics*. Springer, Verlag, 2006.
- [10] F.W. Doss, Structure in Radiative Shock Experiments, Ph.D. thesis, University of Michigan, 2011
- [11] C.C. Kuranz, B.E. Blue, R.P. Drake, H.F. Robey, J.F. Hansen, J.P. Knauer, M.J. Grosskopf, C. Krauland, D.C. Marion, Dual, orthogonal, backlit pinhole radiography in OMEGA experiments, *Rev. Sci. Instrum.* 77 (2006) 10E327–10E327-4.
- [12] G. Tóth, Y. Ma, T.I. Gombosi, Hall magnetohydrodynamics on block-adaptive grids, *J. Comput. Phys.* 227 (2008) 6967–6984.
- [13] M.J. Berger, P. Colella, Local adaptive mesh refinement for shock hydrodynamics, *J. Comput. Phys.* 82 (1989) 64–84.

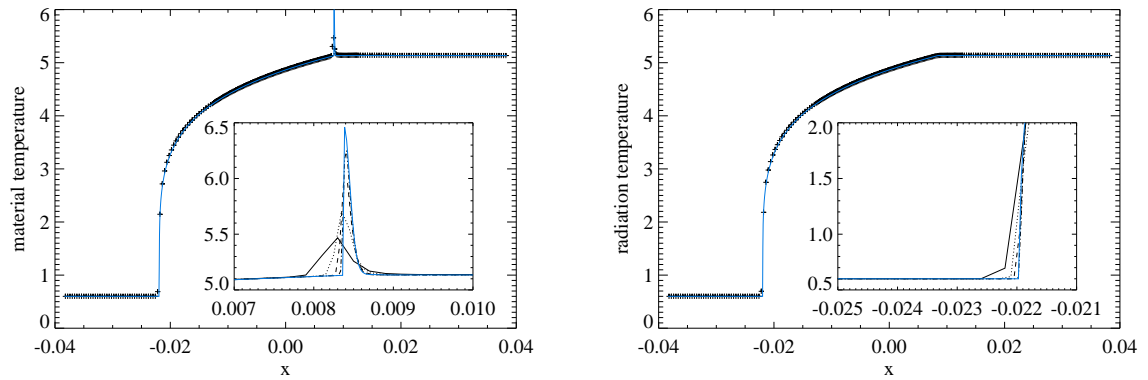


Figure C.16: Material (left panel) and radiation (right panel) temperature at the final time for the Mach 5 radiative shock tube problem rotated on a non-uniform grid. The blue line is the reference solution obtained from [16]. The insets show the temperature jump at the hydro-shock (left panel) and the radiation precursor front (right panel).

- [14] M.G. Edwards, Elimination of adaptive grid interface errors in the discrete cell centered pressure equation, *J. Comput. Phys.* 126 (1996) 356–372.
- [15] B. van der Holst, W.B. Manchester IV, R.A. Frazin, A.M. Vásquez, G. Tóth, T.I. Gombosi, A data-driven, two-temperature solar wind model with Alfvén waves 725 (2010) 1373–1383.
- [16] R.B. Lowrie, J.D. Edwards, Radiative shock solutions with grey nonequilibrium diffusion, *Shock Waves*, 18 (2008) 129–143.